A Meta-Model for Tubercle Design of Wing Planforms Inspired by Humpback Whale Flippers

A. Taheri

Abstract—Inspired by topology of humpback whale flippers, a meta-model is designed for wing planform design. The net is trained based on experimental data using cascade-forward artificial neural network (ANN) to investigate effects of the amplitude and wavelength of sinusoidal leading edge configurations on the wing performance. Afterwards, the trained ANN is coupled with a genetic algorithm method towards an optimum design strategy. Finally, flow physics of the problem for an optimized rectangular planform and also a real flipper geometry planform is simulated using Lam-Bremhorst low Reynolds number turbulence model with damping wall-functions resolving to the wall. Lift and drag coefficients and also details of flow are presented along with comparisons to available experimental data. Results show that the proposed strategy can be adopted with success as a fast-estimation tool for performance prediction of wing planforms with wavy leading edge at preliminary design phase.

Keywords—Humpback whale flipper, cascade-forward ANN, GA, CFD, Bionics.

I. INTRODUCTION

HUMPBACK whales (*Megaptera novaeangliae*) are amazing animals. From biological point of view, they belong to cetacean group having evolved streamlined body with some attached fin and flukes to provide maximum swimming performance [1]. Their lifespan is about 45-50 years. Due to the ecological necessity of life in oceans, humpback whales developed some unique features as an individual or in a group, like breaching behavior, generation of the most complex sound among the swimming animals and utilization of a smart bubble net fishing technique, to name a few [2]. Despite their long body length, about 12-18 m, and their heavy body mass, about 30-40 tons, these animals are remarkable swimmers. Compared to other types like gray, white and blue whales, humpback whales need medium range of cruising speed and high feeding maneuverability [1]. To some extend their superior swimming performance is due to their powerful fluke with maximum relative area among the above-mentioned species [1], although this is not all the story.

From hydro-dynamical point of view, high level of maneuverability of these species in turning, rolling and banking is majorly linked with the special topology of their pectoral fines, called 'flippers'. Humpback whales have the longest flipper among all whales (Fig. 1), with a length of about 0.3 of the body length [1], [2]. Fig. 1 shows the planform of a humpback whale flipper [4]. As shown, it

A. Taheri, Ph.D., Division of Applied Computational Fluid Dynamics, Biomimetic and Bionic Design Group, Tehran, Iran (e-mail: taha.bionics @gmail.com).

possess special pattern of tubercles on the leading edge and the trailing edge, which forms peaks and troughs with varying amplitude and wavelength. On the other hand, there exist a net of ventral (throat) grooves (pleats) on the belly part of the animal. This net allows whales to expand their throat like an accordion in the lunge-feeding process [5], [6]. Presence of these grooves modifies external shape of the underside of the animal, even in the non-lunge stage, compared to the smooth body surface and results in some fluid dynamical consequences [11].

Generation of the streamwise vortices is the key factor to understand the flow hydrodynamics over the humpback whale flippers. In fact, two counter-rotating vortices with different vorticity signs are generated by the tubercled leading edge topology on different sides of the trough for any individual protuberance (Fig. 3 (c)) and also a secondary- spanwise flow forms in the leading edge region [7], [8]. It is postulated that higher amount of momentum induced by streamwise vortices results in a softer/flatter behavior in the post-stall region for wings with leading edge undulations. In this perspective, leading edge protuberances resembles vortex generators and can be seen as a passive flow control tool. In the vortex generator concept, a pair of little plates, with diverging configuration for example, is placed on the certain position on the upper surface of the wing to generate two counter-rotating vortices [9]. In general, this system enhances momentum transfer and fluid flow mixing close to the wall and leads to separation delay at high angles of attacks.

In another aerodynamic model proposed by Van Nierop et al. [10], a partial non-uniform downwash generated by the topology of the leading edge contributes to stall delay. They showed that stall is independent of the wavelength of undulations. In their analytical model, flow field is divided into two separate regions; one close to wall, i.e. turbulent boundary layer and another outside of the boundary layer, which is considered in the model, as potential flow [10]. Using the model, they could capture main features of hydrodynamics of planforms with bumpy tubercles. They analytically demonstrated that for both cases of the rectangular and semi-elliptical planform, more flattened lift coefficient curves in the stall region are obtained by increasing amplitude of the leading edge undulations [10].

As mentioned, presence of the ventral grooves can also affect the swimming performance. Fig. 2 shows a schematic view of the ventral grooves on the belly part of a humpback whale body. In real species, the ventral pleat net covers the entire humpback whale belly. As shown in the figure, here ventral grooves on the right-hand side of the body were

omitted in the drawing to create an imaginary-smooth zone (without grooves) for comparison purposes only [11].
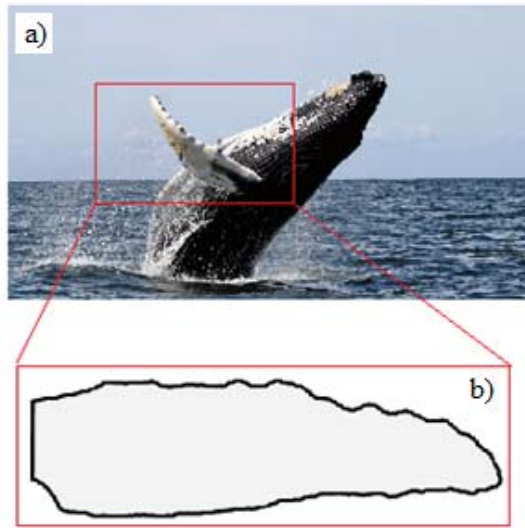

Fig. 1 Humpback whale; (a) breaching behavior [3], (b) flipper planform (reconstructed from a real geometry [4])
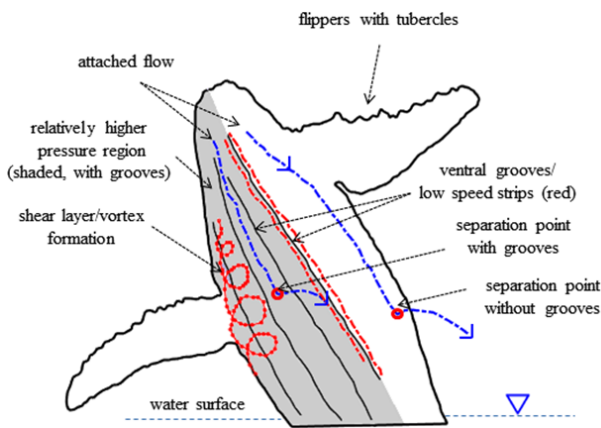

Fig. 2 Schematic of hydrodynamic effects of ventral pleats [11]

Geometrically, ventral grooves can be viewed as semi-parallel lines on the elliptic Riemannian geometry of the belly surface with a positive curvature. Therefore, semi-parallel groove lines (curves) create a diverging-converging pattern involving a varying angle with respect to the longitudinal body axis. As shown in another paper of the present author [11], presence of these ventral pleats leads to the formation of low speed strips and shear layer/vortex on the belly surface; which in turn creates a relatively higher pressure region and higher drag coefficient (gray shaded region in Fig. 2) compared to the case without grooves [11]. In this manner, ventral pleats generate lift and contribute to buoyancy force. In the non-lunge phase, low speed stripes also increase tendency of the flow separation. As also shown, in the case of bubbly flow conditions, e.g. in the bubble net fishing environment, lift generation is suppressed [11].

There exist more interesting lessons considering humpback whale swimming hydrodynamics, however in the present research; focus is on the behavior and design of the wings with wavy leading edge inspired by humpback whale flippers. In the following sections, details are presented.

A. Wing Planform Characteristic Parameters

Basic geometrical parameters adopted in the proposed meta-model for the wing planform design are defined in Fig. 3. In general, for a swept wing, these parameters include: wing span b, taper ratio c_t / c_r, quarter chord sweep angle $\Lambda_{\overline{c}/4}$ (Fig. 3 (a)).

a) Swept wing planform

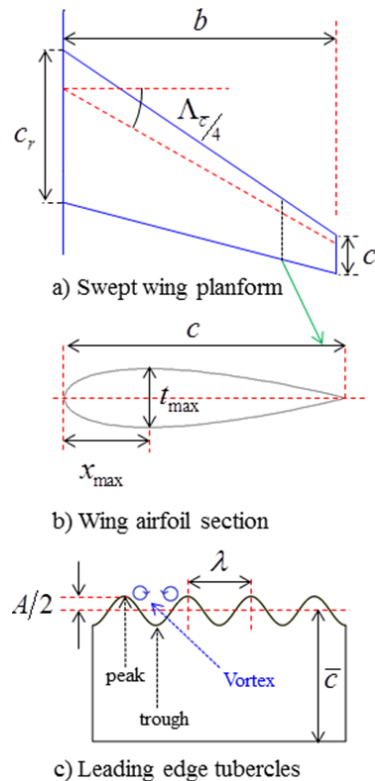b) Wing airfoil section

c) Leading edge tubercles

Fig. 3 Wing planform anatomy and its characterizing parameters

To represent geometry of the wing airfoil section, chord length c, maximum thickness t_{max} and position of the maximum thickness x_{max} are considered (Fig. 3 (b)). In the case of wavy wing planform with the leading/trailing edge tubercles/undulations, two other parameters should be included, namely: amplitude A and wavelength λ of the leading edge undulations (Fig. 3 (c)). In this case chord, length varies in the spanwise direction; therefore average chord is replaced by the mean chord $\overline{c}$ (Fig. 3 (c)).

B. Experimental and Numerical Studies in the Literature

During the recent decade, effects of the leading edge waviness on the wing performance have been studied both numerically and experimentally; Tables I and II summarize these studies, respectively. As it is clear in Table I, flow over

different planforms, majorly with rectangular shape, has been simulated [12]-[29]. Aspect ratio, $AR = b/\overline{c}$ range of the planforms is limited from 0.45 to 4.33 (and theoretically infinite for 2D flow condition).

Symmetric and non-symmetric NACA airfoils with leading edge tubercles have been studied numerically in the literature with non-dimensional amplitude and wavelength of undulations ranging as $A/\overline{c} \approx$ 0.0125 to 0.2 and $\lambda/\overline{c} \approx$ 0.016 to 2.44, respectively. The adopted airfoils include: 0012, 0018, 0020, 0021, 2412, 63_4-021 and LS(1)-0417, and also NREC S809 and FX 63-137 airfoil sections [12]-[29].

Reynolds number range based on the free stream velocity and mean chord length is limited from 800 to 10^6. The lower limit of Re, i.e. 800, is lower than transition to turbulence state, although large enough to grow first spanwise instabilities before transition to turbulence [12]. The upper limit of Re, i.e. 10^6, corresponds to turbulence state. Humpback whales approximately experience Re of the order of 10^6 [4]. For turbulence treatment, different strategies have been applied like DNS without any modeling ad-hoc to LES which only resolves larger eddies greater than the filter size (typically cell size), hybrid RANS/LES methods like DDES, RSM treatment and also RANS methods including: $k - \varepsilon$, SA, $k - \omega\ SST$ and transitional models, like $SST\ \gamma - Re_\theta$.

As shown in Table I, for numerical solution of the continuity and Navier-Stokes equations, different solvers have been adopted in the literature, such as: STAR-CCM+, ANSYS-Fluent and CFX, PHOENICS, Nectar++, OpenFOAM, SolidWorks and also in-house codes; each one with its own advantages and limitations. In general, some deviations exist in performance predictions of the wavy planforms between experimental and simulation results in the literature due to limitations of CFD simulations to replicate the flow physics. On the other hand, since 2004 experimentally intensive campaigns of flow measurements have been conducted by researchers to study performance and flow topology of wing planforms with the leading edge undulations as one can see in Table II. In these experiments, effects of different design parameters have been considered, like: airfoil type, airfoil thickness, Re, AR, $A/\overline{c}$ and $\lambda/\overline{c}$ [30]-[40]. Experiments were majorly performed using rectangular planforms without wing taper, although idealized flipper shapes with/without wing taper were also studied in the literature so far [31], [34], [37], [39], [40].

In the experiments, water tunnel [32]-[34], [37] and wind tunnel [24], [30], [31], [35], [36], [38]-[40] facilities were adopted to pursue the goals. To measure forces and moments in the experiments, strain gage load cells were typically utilized. For flow velocity and pressure measurements, different techniques have been applied like: Pitot tube micro manometer system [24], LDV [32], [33], PIV [34], [35]; hot-wire [35], surface static pressure taps [35]; and for flow topology visualizations following visualization techniques have been applied, like: Hydrogen bubble [35], [39], [40], tuft [32], [38], dye [32] and oil [38]. In addition, acoustic measurements have been performed by Hansen to quantify acoustic effects of the leading edge indicating that wings with tubercled planforms can efficiently eliminate tonal noise [35].

TABLE I
NUMERICAL STUDY SUMMARY

Author	Turbulence treatment	Solver	Re	AR	Airfoil	planform	$A/\overline{c}$	$\lambda/\overline{c}$	Ref.
Favier et al.	DNS	In-house code	800	2	NACA 0020	Rectangular	0-0.1	0.25-2.0	[12]
Arai et al.	LES	FrontFlow code	1.38×10^5	1.6	NACA 0018	Rectangular	0.05	0.08, 0.016	[13]
Cai et al.	RANS-SA k-ω SST	ANSYS-Fluent	1×10^5	3.5	NACA 63_4-021	Rectangular	0.1	0.25	[14]
A.K. Malipeddi	DES-SA DES-SST k-ω	ANSYS -Fluent	5.7×10^5	1	NACA 2412	Rectangular	0.025, 0.05	0.25, 0.5	[15]
Skillen et al.	LES	OpenFOAM	1.2×10^5	0.45	NACA 0021	Rectangular	0.015	0.11	[16]
Esmaeili et al.	RANS, DDES DDES-LRC k-ε	ANSYS -CFX	1.4×10^5	1, 1.5	NACA LS(1)-0417	Rectangular	0.12	0.5	[17]
K. R. Atkins	k-ω SST LRR-RSM	STAR-CCM+	1.5×10^5	0.47	NACA 0021	Rectangular	0.0075	0.11	[18]
Asli et al.	DES-SST k-ω	ANSYS -CFX	10^6	2D	NREC S809	Rectangular	0.025	0.25	[19]
Rostamzadeh et al.	SST γ-Re$_\theta$	ANSYS-CFX	1.2×10^5	2D	NACA 0021	Rectangular	6.5°	0.43	[20]
Cai et al.	RANS-SA	ANSYS-Fluent	1.83×10^5	2	NACA 63_4-021	Rectangular	0.12, 0.025	0.5	[21]
Solís-Gallego et al.	k-ω SST	ANSYS-Fluent	3.5×10^5	3.28	NACA 63_4-021 FX 63-137	Rectangular	0.1, 0.2	1.67	[22]
Maksoud and Ramasamy	k-ε	PHOENICS CFD	2.4×10^5	2	NACA 63_4-021	Rectangular	0.025, 0.05, 0.12	0.25, 0.5, 1.0	[23]
Chen et al.	k-ω SST	STAR-CCM+	1.23×10^5	1,2,3	NACA 0012	Rectangular	0.1	0.25	[24]
Pedro and Kobayashi	DES-SA	ANSYS-Fluent	5×10^5	4.33	NACA 0020	Idealized flipper	NA	NA	[25]
Weber et al.	SA, k-ε k-ω SST	STAR-CCM+ SolidWorks	5.2×10^5	4.33	NACA 0020	Idealized flipper	NA	NA	[26]
Lohry et al.	k-ω SST	In-house code	5×10^5	0.8	NACA 0020	Rectangular	0.04	2.44	[27]
Joy et al.	k-ω SST	ANSYS-Fluent	1.4×10^4	4	NACA 63_4-021	Rectangular	0.12	0.25, 0.5	[28]
Serson et al.	DNS	Nectar++	1000	1	NACA 0012	Rectangular	0.0125- 0.2	0.25-1.0	[29]

TABLE II
EXPERIMENTAL STUDY SUMMARY

Author	Re	AR	Airfoil	Planform	$A/\overline{c}$	$\lambda/\overline{c}$	$\Lambda_{\overline{c}/4}$	Ref.
Miklosovic et al.	5.2×10^5	4.33	NACA 0020	Idealized flipper	NA	NA	NA	[30]
Miklosovic et al.	$2.7 \times 10^5 - 6.3 \times 10^6$	3.3	NACA 0020	Rectangular Idealized flipper	0.04	0.41	0	[31]
Custodio and Johari	1.83×10^5	1.99, 2.99 Semi/full span	NACA 63$_4$-021	Rectangular	0.025, 0.05, 0.12	0.25, 0.5	0	[32] [33]
M. J. Stanway	$4.4 \times 10^4 - 1.2 \times 10^5$	4.132	NACA 0020	Idealized flipper	NA	NA	NA	[34]
K. L. Hansen	1.2×10^5	3.5, 7 Semi/full span	NACA 0021 NACA 65-021	Rectangular	0.03, 0.06, 0.11	0.11, 0.21, 0.43, 0.86	0	[35]
Chen et al.	1.23×10^5	1, 2, 3	NACA 0012	Rectangular	0.05, 0.1, 0.15	0.25	0	[24]
J. Borg	1.3×10^5	2.5	NACA 0021	Rectangular	0, 0.05, 0.12	0.25, 0.33, 0.5	0	[36]
Custodio et al.	$9 \times 10^4 - 4.5 \times 10^5$	2.0, 2.15, 4.33 Semi/full span	NACA 63$_4$-021	Idealized flipper Rectangular	0.025, 0.05, 0.12	0.25, 0.5	0, 26º	[37]
A. A. D. Paula	$5 \times 10^4 - 2.9 \times 10^5$	3, full span	NACA 0012 NACA 0020 NACA 0030	Rectangular	0.03, 0.11	0.11, 0.4	0	[38]
M. Bolzon	2.2×10^5	2.7	NACA 0021	Rectangular, tapered	0.15	0.86	35º	[39] [40]

To the present date, each experimental campaign provided a piece of puzzle to complete global map of the tubercled wing performance; although there are some missing zones. As one can see in Table II, effects of a broad mutual change in design parameters of a rectangular wing with wavy leading edge (shown in Fig. 3) have been quantified in the aforementioned experiments [30]-[40]; like change in Re [37], [38], change in aspect ratio [32], [33], [35], [37], [38], change in airfoil thickness [38], change in undulation amplitude [24], [32], [33], [35]-[38], change in undulation wavelength [32], [33], [35]-[38] and finally change in quarter chord sweep angle [37], [39], [40]. In this paper, having on hand all these individual sets of data, a cascade-forward ANN is designed and trained in a supervised manner using all aforementioned experimental data to generalize performance prediction map of the tubercled wings. In the following section, details are presented.

II. META-MODEL DESIGN

In general, ANN is a promising technique that mimics brain functionality in learning via adjustment of synaptic weights and bias of nonlinear neurons to generalize data sets with missing zones and also to predict systems involving high level of non-linearity. Here in the case of performance prediction of tubercled planforms, i.e. lift and drag coefficient estimations, a highly nonlinear relation exists between the design parameters and outputs as observed in the experimental data sets [30]-[40]. Therefore, applying ANN concept in the present application can be fruitful.

A. Designed Cascade-Forward ANN

In this section, a supervised cascade-forward ANN is designed and trained by experimental data in MATLAB environment [41] to estimate lift and drag coefficients for tubercled planforms; the resultant matrix of the adjusted weights and bias of the ANN can be used in preliminary design phase as a fast-estimation tool for performance prediction. Fig. 4 shows architecture of the designed ANN.
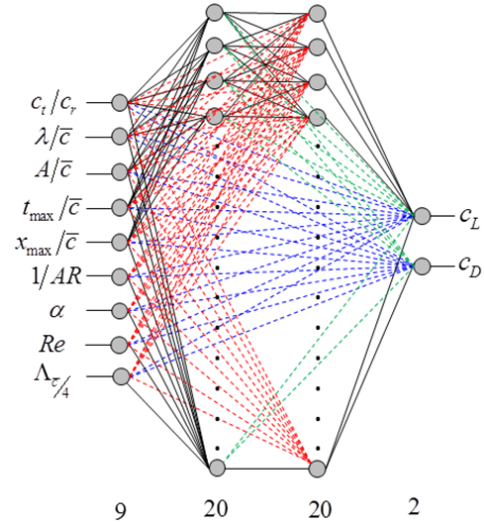

Fig. 4 Topology of the designed cascade-forward ANN

As one can see in the figure, the designed cascade-forward ANN has a configuration with 9 neurons in the input layer corresponding to 9 dimensionless wing design parameters, including: taper ratio c_t/c_r, wavelength and amplitude ratios of the leading edge undulations i.e. $\lambda/\overline{c}$ and $A/\overline{c}$, maximum thickness ratio $t_{max}/\overline{c}$, maximum thickness position ratio $x_{max}/\overline{c}$, inverse of aspect ratio $1/AR$ and wing planform quarter chord sweep angle, namely $\Lambda_{\overline{c}/4}$. These characteristic parameters along with Reynolds number Re and angle of attack (AoA), α, can effectively describe fluid dynamical state of a wavy planform. The ANN involves two neurons in the output layer corresponding to lift c_l and drag c_d coefficients and also 2 hidden layers with 20 neurons per each layer. In cascade-forward ANN, hidden layers at the beginning of calculations are empty and neurons are gradually added one by one to finally meet 20 neurons per layer.
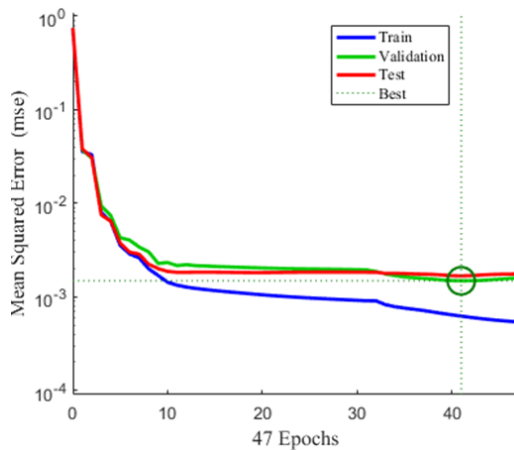
Fig. 5 Learning history of the designed cascade-forward ANN

As shown in Fig. 4, cascade-forward ANN is similar to typical feed-forward nets, although there are more connections between the neurons in different layers [42]; in other words, for instance, input layer neurons involve synaptic connections to all neurons of the net in the following layers including hidden and output layers. With this specific configuration, cascade-forward ANN with two or more hidden layers along with enough case-dependent number of neurons in hidden layers can theoretically represent any complex relation between input and output data.

As mentioned earlier, to form the training data set for the net, experimental lift and drag coefficient curves available in the literature (Table II) were digitalized and assembled to form a comprehensive database. The database involves 2100 sets of 9 inputs and 2 outputs pair. In this regard, only experimental data conducted over rectangular (not idealized flipper) wing planforms were considered [24], [31]-[33], [35], [36], [38]-[40]. It is worth to emphasize that to increase stability of the ANN learning process, normalized values of inlet and output parameters were fed to the ANN.

B. ANN Performance

After the training phase, the designed ANN approximates the relation between the input parameters and the output lift/drag coefficients of the wavy planform. In the process, weight and bias are adjusted; the designed cascade-forward net uses Levenberg-Marquardt optimization back-propagation method with 2nd order training speed faster than many traditional feed-forward nets, but at the expense of higher memory demand [41]. The net also uses random data division strategy and mean square error (MSE) estimations between target and output vectors to define cost function of the net.

In the learning process, about 20% of the comprehensive data set is continuously sampled for validation and test purposes at each epoch. In general, validation and test vectors have similar functionality to monitor convergence of the learning process; although they are separate sets both sampled from the original dataset. In fact, validation vectors are used for termination of the learning process when convergence is achieved, but test vectors are only adopted as an indicator to

further evaluation of the net generalization performance without any role in learning process termination [41].

Fig. 5 depicts learning history curves for training, validation and test data sets. Best validation performance is obtained as 0.0014823 at epoch 41. Total convergence is achieved when MSE (or cost function) reaches to a threshold level equals to 5×10^{4}.

Fig. 6 shows error histogram of the designed cascade-forward ANN for training, validation and test data sets. As one can see in the figure, favorably major portion of error samples in the learning process locates close to zero (zero error line, i.e. orange vertical line). There also exist smaller portions of samples on the left (Targets<Outputs) and right (Targets> Outputs) wings of the zero error line. Overall, the error distribution shows well-converged state of the cascade-forward ANN in the present application.
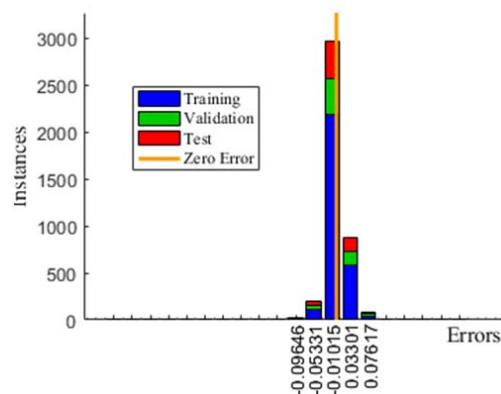

Fig. 6 Error histogram of the designed cascade-forward ANN in the learning process with 20 bins (Error=Targets-Outputs)

To further investigate performance of the designed ANN, regression between Targets and Output for training, validation and test data sets has been performed in Fig. 7. The ideal case is obviously a line with 45° slope angle (Target=Output) in the solution space, i.e. Target-Output plane. As one can see in the figure, data samples for all data sets are located around the ideal regression line with higher density on the line which produces 0.97-0.99 slope-factors. Considering large number of data samples, only few samples are off-line for all training, validation and test data sets, thanks to the optimized well-converged learning process.

After global investigation of the ANN learning process, capability of the trained ANN in lift and drag coefficient predictions for a sample validation data set is assessed in Fig. 8. In the experiment conducted by Borg [36], a rectangular planform with NACA 0021 airfoil section has been tested in a wind tunnel at $Re = 1.3 \times 10^{5}$; the base wing planform has no taper with $AR = 2.5$ and involves leading edge undulation specifications as $A/\overline{c} = 0.12$ and $\lambda/\overline{c} = 0.5$ [36].

Fig. 8 shows prediction results of the trained cascade-forward ANN for lift and drag coefficients along with c_l/c_d parameter compared to the experimental counterparts for the described planform [36]. Drag coefficient is predicted

precisely; small deviation in lift coefficient prediction exists ranging from AoA= $8°$ to $12°$, where a very radical variation in a short AoA interval exists in the experimental data. In addition, some deviations in prediction of c_l/c_d parameter are observed on the same range of AoA. As one can see in the figure, the trained ANN provides impressive results and is capable to capture major nonlinear behavior of the tubercled wing planforms.
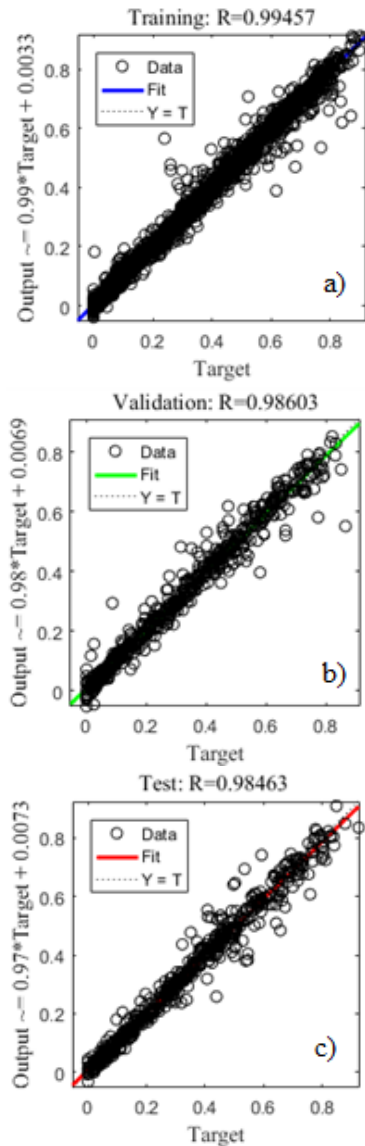
includes almost all available experimental data conducted on the wavy planforms to the date, although the proposed ANN implementation has the capability to add future experimental data by simply adding new data to its database with no restriction and no modification. In this manner, accuracy of the trained ANN predictions increases specially on the parameters with more experimental data coverage.
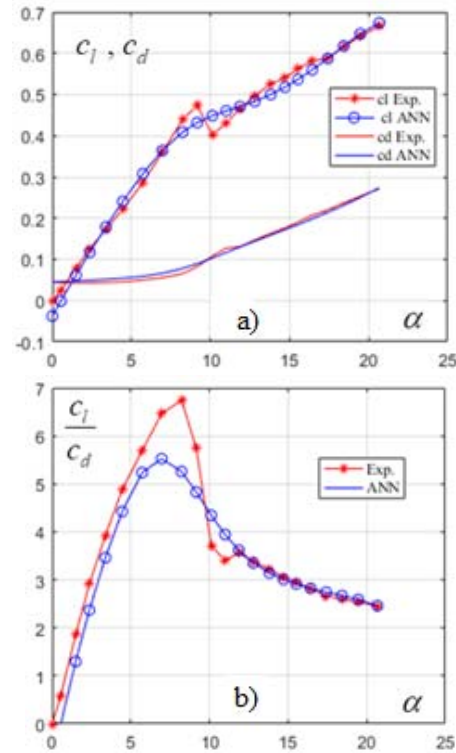

Fig. 7 Cascade-forward ANN prediction regression for (a) training data set, (b) validation data set, and (c) test data set

Fig. 8 Comparison of (a) lift and drag coefficients, and (b) lift to drag ration of a wavy leading edge planform obtained from the designed ANN and experimental measurement counterpart [36]]

As a result, the trained cascade-forward ANN can be utilized as a fast estimation tool to predict c_l and c_d parameters in preliminary design phase of the tubercled wing planforms. This is simply done by performing computationally efficient matrix manipulations. Furthermore, as mentioned earlier, the comprehensive database utilized for ANN training

III. DESIGN OPTIMIZATION USING GENETIC ALGORITHMS

Having on hand, all weights and bias of the trained ANN expressed in a frozen matrix, a fitness function typically utilized in any optimization technique can be efficiently evaluated. In general, to obtain more accurate optimization results in the case of systems with high degree of nonlinearity and also systems with lack of experimental data in given zones in the input hyperspace, it is recommended to use constrained zonal optimization, rather than unconstrained optimization. The hyperspace is constructed as input parameter space, here a 9 dimensional (9D) space corresponding to 9 inputs of the problem.

To demonstrate the idea of zonal optimization in the present study, a 3D fractional rectangular space in the 9D hyperspace around an experimental data set conducted by Chen et al. [24] is considered for optimization. Constrains of the optimization is applied as below:

$$0.03 \leq \lambda/\overline{c} \leq 0.25$$
$$0.03 \leq A/\overline{c} \leq 0.15 \tag{1}$$
$$5° \leq \alpha \leq 40°$$

The above subspace defines a 3D cube in the 9D hyperspace. All other inputs are considered as the planform parameters in the experiment: $c_t/c_r = 1$, $AR = 1$ and $\Lambda_{\overline{c}/4} = 0$; airfoil parameters: $t_{max}/\overline{c} = 0.12$ and $x_{max}/\overline{c} = 0.3$, and Reynolds number as 1.2×10^5. For the optimization, genetic algorithm (GA) method, which belongs to evolutionary optimization techniques, is utilized in MATLAB environment. In general, GA mimics natural biological evolution based on the principle of survival of the fittest species [43]. In the technique, a fitness function defined based on given variables is minimized; in the case of tubercled planform different combination of c_l and c_d can be considered for optimization or minimization. In the present study, the following expression is considered as fitness function to avoid singularity at the origin:

$$fitness = \sqrt{\frac{c_d^2 + 1}{c_l^2 + 1}} \tag{2}$$

For the present optimization problem, GA population size and tolerance is considered as 10^3 and 10^{-10}, respectively. Fig. 9 shows the fitness function evolution over time for best samples and averaged values. The algorithm stops if the average relative change in the best fitness value is less than or equal to the above-defined tolerance. The optimum values of the parameters in this case are obtained as: $\alpha \approx 28.6°$, $\lambda/\overline{c} \approx 0.19$ and $A/\overline{c} \approx 0.03$.
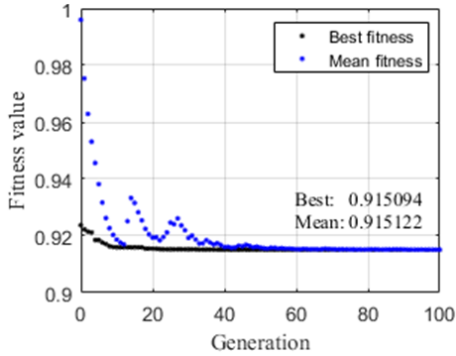

Fig. 9 GA optimization for 3 variables: $A/\overline{c}$, $\lambda/\overline{c}$ and α

The strategy is capable to be extended to more variables, i.e. 4-9 input variable optimizations with/without constrains. The crucial factor is availability of experimental data with maximum coverage to achieve well-trained ANN along with applying zonal optimization strategy. In the next sections, to gain better insight about the physics of the problem, flow over tubercled wings is simulated for the optimized rectangular

planform and also for a real humpback whale flipper. Details are presented in the following sections.

IV. NUMERICAL SIMULATION OF WAVY PLANFORMS

In this section, flow field over aforementioned optimized rectangular planform with wavy leading edge topology along with a real humpback whale flipper model are numerically simulated at different AoAs to obtain performance curves as well as to grasp details of the flow field topology like separation formation. In all simulations, tubercled wings are kept at a fixed position in space, i.e. in x-z plane and effect of AoA (α) is included via setting a freestream blowing angle (Fig. 10).
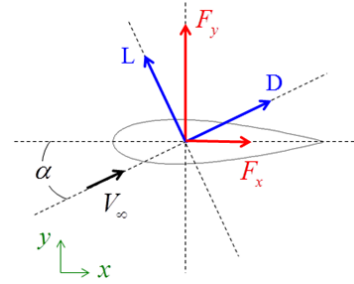

Fig. 10 Airfoil section coordinate system

As one can see in Fig.10, there is a rotational transformation to translate forces in x and y directions (calculated directly in the simulations by the goal settings) to lift and drag forces. Inflow velocity at the inlet plane is also imposed via x and y components of the velocity defined by a given Re; while freestream uniformly flows on the wing in z-direction by imposing null lateral velocity at the inlet plane, as below:

$$u_x^{inflow} = V_\infty . \cos(\alpha)$$
$$u_y^{inflow} = V_\infty . \sin(\alpha) \tag{3}$$
$$u_z^{inflow} = 0$$

It is also worth mentioning that to batter capture flow behavior over wavy planforms in the after-stall region, AoA range applied for simulations is considered as $\alpha \approx 0 - 40°$, with lower resolution in low AoA and higher resolution in the stall region.

A. Tubercled Rectangular Wing

In this section, a total number of 15 simulations have been performed to obtain performance curve of the tubercled wing with rectangular planform as well as flow field details.

1. Geometry and Computational Grids

The planform in this section has a sinusoidal undulation pattern with $\lambda/\overline{c} \approx 0.19$ and $A/\overline{c} \approx 0.03$ at the leading edge as proposed by the optimization strategy (Section III). The wing has mean chord as $\overline{c} \approx 0.1$ m and span as $b \approx 0.104$ m with NACA 0012 airfoil section generated here by XFOIL 6.99 code. The geometry has been numerically constructed in the

SolidWorks Environment [44]. Computational grids for the external flow simulations here were also constructed using SolidWorks meshing tools with adaptive mesh-clustering capability near complex geometrical features (e.g. tubercles) and also in the boundary layer zone (with minimum 10 nodes close to the wall in the boundary layer zone). Fig. 11 depicts the geometry along with the mesh and computational domain. Fig. 12 also shows grid generated around the airfoil section of the wing in the middle section with clustering near the wall.
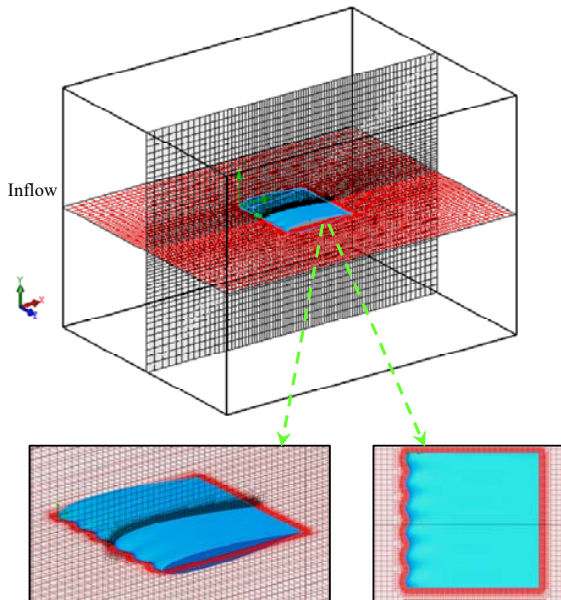
Fig. 11 Tubercled wing grid and computational domain

As shown in Fig. 12 near wall is completely resolved to the wall due to the computational demand of the adopted turbulence treatment utilized in the present study (explained in the next subsection). After performing tests, a converged grid with about 1.5 million elements has been utilized for the simulations. It is worth mentioning that simulations resolving to the wall for multiple operating points adopted in this study are computationally costly; therefore, there is always a trade-off between size of the computational domain, mesh resolution and a desired accuracy level. As one can also see in Fig. 11, computation domain is considered large enough about one and two span in streamwise and lateral directions to minimize boundary effects.
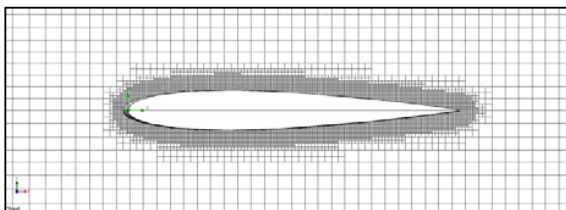

Fig. 12 Cross-sectional adaptive grid around NACA 0012 airfoil

2. Solver, Turbulence Treatment and Settings

Navier-Stokes, continuity and turbulence model governing equations of the fluid (water) flow motion over the planforms are solved using SolidWorks Flow Simulation (SFS) solver [44], [45]. Reynolds number of the flow for all AoAs is about 1.2×10^5 at upper transitional region to the turbulent regime. Turbulent/transitional flow in the present application is treated using Lam-Bremhorst low-Reynolds number $k - \varepsilon$ model (LB LRN $k - \varepsilon$, hereafter) resolving to the wall [46]. The modified $k - \varepsilon$ model is different with the traditional $k - \varepsilon$ turbulence model; in LB LRN $k - \varepsilon$ approach, damping functions are introduced and calculated as functions of minimum distance to the wall. The model needs at least 10 nodes in the direction normal to the wall-surface in the boundary layers to efficiently approximate these high-gradient zones.

In general, SFS uses 2nd order discretization in time and space to handle the derivative terms. SFS solver numerically solves governing equations of the fluid flow motions by an operator-splitting technique and utilizes a SIMPLE-like approach to treat pressure-velocity decoupling issue [44], [45]. In addition, the solver solves asymmetric linear system of the discretized equations approximated from the momentum/ turbulence models with a preconditioned conjugate gradient method and an incomplete LU factorization preconditioning. On the other hand, symmetric pressure-correction system of equations is solved by applying a multigrid technique [45].

As mentioned earlier, for numerical simulations three components of the inflow velocity (3) is set at the inflow section (Fig. 11). Furthermore, 'outflow' condition is applied for other boundaries. For simulation convergence, in addition to the velocity and pressure variables, two predefined goal functions including F_x and F_y forces are monitored to achieve a converged state. In SFS solver, convergence criteria are set automatically by the solver based on dynamic calculation of dispersion of the goal functions [26], [44].

At each AoA, a steady-state LB LRN $k - \varepsilon$ flow simulation is performed and converged flow field and forces are saved for post-processing. Results are presented in the following.

3. Results

Fig. 13 shows lift and drag coefficient curves obtained from numerical simulations of the optimized tubercled rectangular wing. For comparison purposes, a similar experimental data conducted by Chen et al. have been also plotted for clean and tubercled wings in the figure [24]. In the experiment, all parameters like Reynolds number, aspect ratio, etc. are the same with the optimized planform with little difference in leading edge undulation pattern as $\lambda/\overline{c} \approx 0.25$ (0.19 in the simulation) and $A/\overline{c} \approx 0.05$ (0.03 in the simulation) in the 'Wavy Exp.' case and also no leading edge undulations in the 'Clean Exp.' case. As one can see in Fig. 13, both numerical performance coefficients are predicted comparable to the experimental data; although the optimized planform exhibits higher lift coefficient in AOA range from $10°$ to $30°$. This can be partially explained by small difference in tubercle undulation geometrical parameters between the optimized planform and its experimental counterpart. The optimized planform desirably shows superior performance in this range.
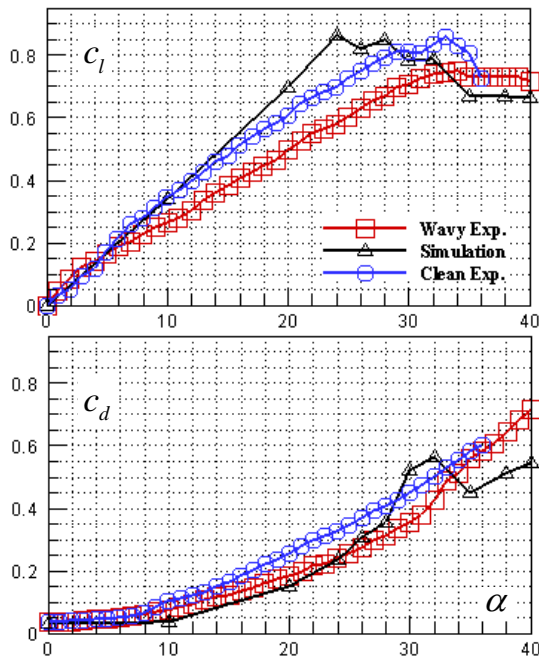
Fig. 13 Tubercled rectangular wing performance curves

Drag coefficient variations for CFD and experimental data are also shown in Fig. 13. Overall, drag coefficient values are in the same range for both cases with wavy planforms. As one can see, up to $24°$, both curves behave almost the same; after this point, numerical curve oscillates around the experimental curve. This is linked to the formation of separation bubble on the optimized rectangular planform as shown in Fig. 14. In the figure, flow pathlines over the optimized planform obtained from the numerical simulations are presented at three different AoAs. As one can see in the figure, for $\alpha = 24°$ pathlines are well-attached on the wing surface; wing tip vortices also form at two ends of the wing due to the pressure difference present on the top and bottom of the planform in accordance to the finite wing aerodynamic theory. As shown in Fig. 14, $\alpha = 24°$ is the onset of separation bubble formation on the top surface of the planform.

The point $\alpha = 24°$ can be considered as the beginning of stall region. It is interesting to mention that by increasing AoA, separation bubble grows and ultimately a relatively large recirculating separation bubble, covering whole the wing, forms on the top surface of the optimized planform at $\alpha = 35°$ AoA. Small values of shear stress in this recirculating separation zone explain lowering of the drag coefficient for the optimized planform at $\alpha = 35°$, as depicted in Fig. 13. As one can observe in Fig. 14, at this high AOA wing tip vortices are deflected and getting bundled due to formation of the large separation bubble and also short wing span length for the present planform case. At this AoA, separation strips clearly form in the tubercle troughs as shown in Fig. 14. It is also important to notice that although separation bubble forms for AOA higher than $24°$, the tubercled wing maintains relatively high level of lift coefficient in the post-stall region (Fig. 13),

due to the higher level of mixing created by the wavy leading edge pattern. In this manner, the wavy planform exhibits a flat behavior for lift coefficient in the post stall region, i.e. in the range $24° < \alpha < 40°$, as shown in Fig. 13.

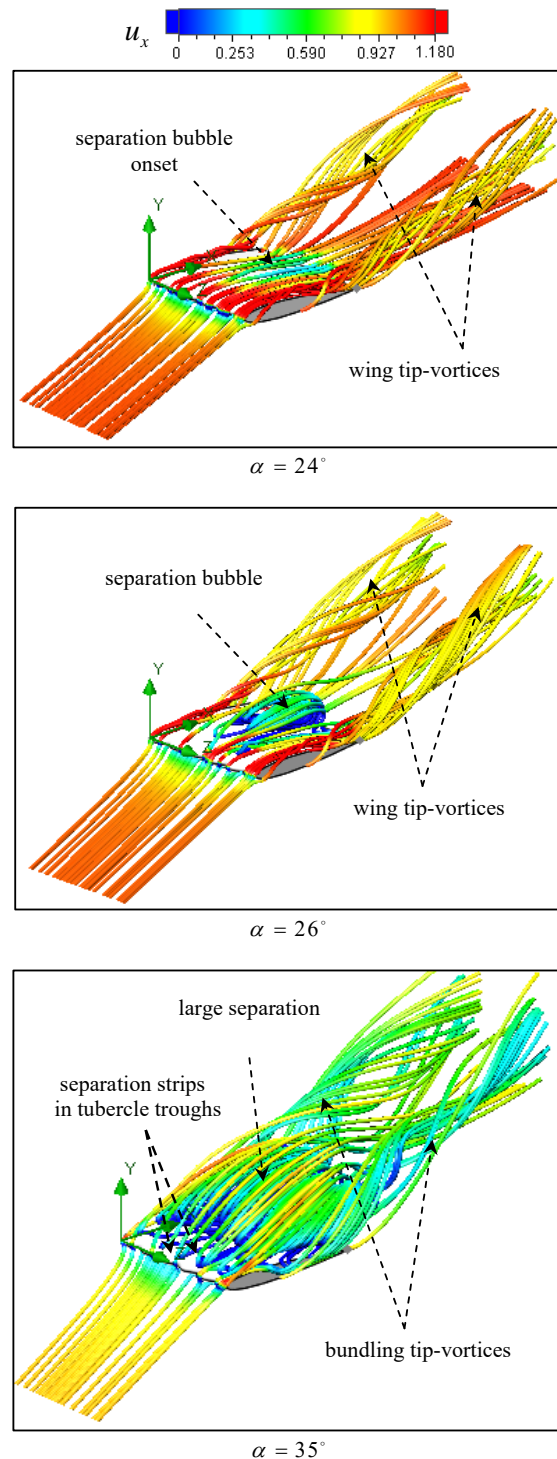$\alpha = 24°$

$\alpha = 26°$

$\alpha = 35°$

Fig. 14 Pathlines over the tubercled wing at different AoAs

To further investigate the problem, streamlines on two trough and peak sample planes perpendicular to the planform at $z = 3\lambda/4$ and $z = 13\lambda/4$ were extracted from the numerical simulation at $\alpha = 40°$, as shown in Fig. 15.
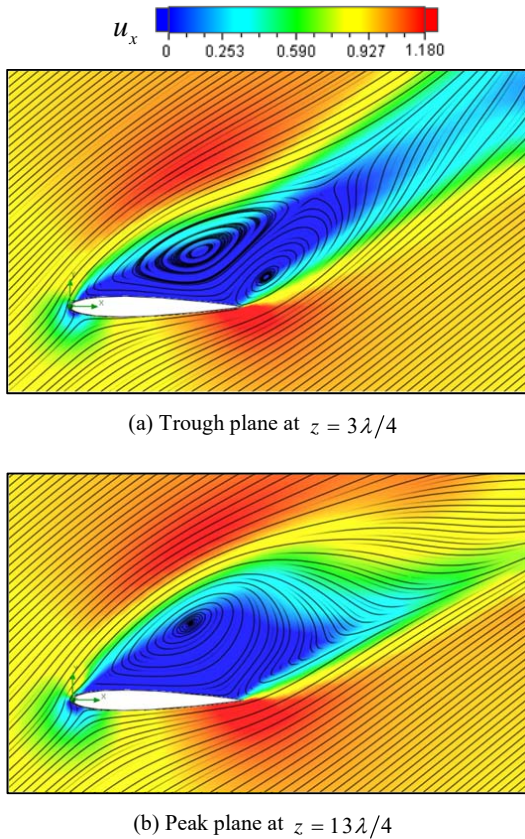

(a) Trough plane at $z = 3\lambda/4$

(b) Peak plane at $z = 13\lambda/4$

Fig. 15 Streamline patterns in trough and peak sample planes of the tubercled wing at high AoA, $\alpha = 40°$

As one can see, in the trough plane, two counter-rotating vortical zones form: one starting at the leading edge and another one close to the trialing edge of the wing section; while for the selected peak plane, only one recirculating region forms covering whole the wing surface at this AoA. Variations also exist between other peak and trough in lateral direction indicating presence of a fully 3D complicated flow over the tubercled wing surface.

To see fluid particle motions under hidden structures formed in the flow field especially in the separation bubble region, a tracer particle study was performed. In this regard, tracer particles, here ethane spherical particles with 0.0001 m diameter, are continually released from the wing surface and convected downstream by the background flow field. In contrast to ideal tracers, real tracers applied here have mass and do not have the same velocity as local flow; therefore, equations of motion for those particles under a given velocity field are solved. For the calculations, ideal reflection has been applied for fluid particle-solid interactions, e.g. in the recirculation zones. Dynamical motions of the tracer particles

showed complicated hidden flow field structures over the tubercled wing, especially in the recirculation zone. Fig. 16 shows a snapshot of the tracer motions colored by the axial velocity of particles. As shown in the figure and also in a movie generated by the present particle study, tracer particles outside of the separated region majorly follow structure formed by bundling tip-vortices in helical-like motions, while particles in the separated zone or close to it exhibit some chaotic recirculating motions and then pass downstream.
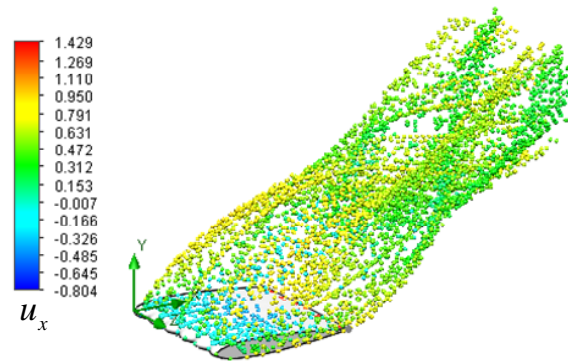

Fig. 16 Tracer particle dynamics over the tubercled wing at high AoA, $\alpha = 40°$

At the end of this section, it is also worth mentioning that for all simulations, wing surface was considered as an ideal surface without roughness. Before starting the comprehensive simulation campaign, effect of roughness on performance prediction of the tubercled wing was also considered to find the optimum setting for the upcoming simulations. In this regard, flow simulations on the wing with surface roughness as 0.01, 0.1 and 0.61 microns (the latter, corresponding to commercial steel) at $\alpha = 30°$ have been conducted with almost no effect on the wing performance predictions.

B. Real Humpback Whale Flipper Model

So far, only tubercled wings with uniform amplitude and wavelength of leading edge undulations were considered in this paper. As stated before, real humpback whale flippers possess a more complicated shape with non-uniform tubercle pattern having variable amplitude and wavelength, as already shown in Fig. 1 [4]. Here in the final section, flow over a real humpback whale flipper model with 0.5 m span and about 0.1 m mean chord is simulated using SFS at $Re \approx 10^6$, corresponding to the Reynolds number experienced by the flipper in *Megaptera novaeangliae* humpback whale swimming with speed of 1.47 m/s [4]. Details are presented in the following.

1. Geometry and Computational Grids

To construct the flipper model, real planform geometry of a whale flipper [4] is digitalized and then adopted as the wing planform outline (shown in Fig.1). Symmetric airfoil 0021 is also selected for wing assembly due to its similar shape with humpback whale flipper cross section [35]. In the modeling

procedure, middle rib airfoil sections of the wing along with leading edge and trailing edge curves of the planform are imported as a cloud of points with high resolution into the SolidWorks CAD environment and the model is majorly constructed by lofting process. The created geometry resembling a real humpback whale flipper, which is attached to the lateral boundary plane, is shown in Fig. 17.
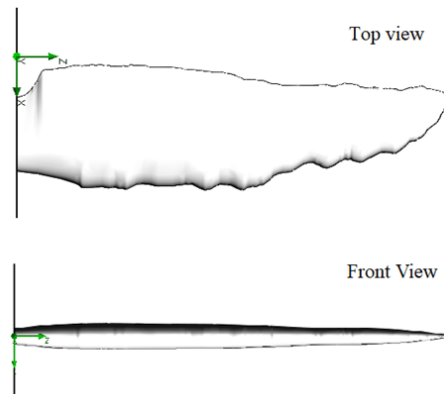

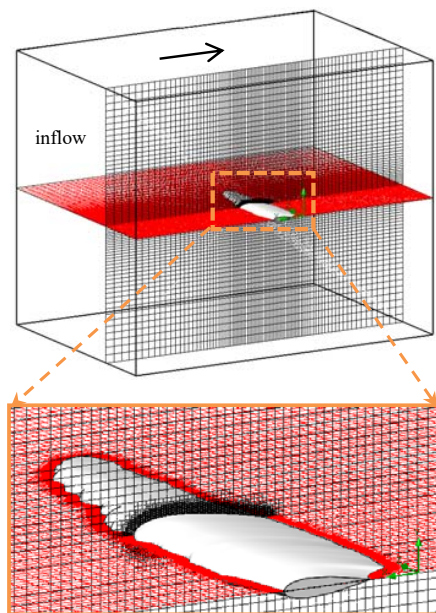Fig. 17 Humpback whale flipper model based on *Megaptera novaeangliae* flipper planform

Fig. 18 Humpback whale flipper grid and computational domain

Similar to the previous case i.e. tubercled rectangular wing, computational mesh for flow simulations was constructed using SolidWorks adaptive meshing tool to capture tubercle geometrical complexities and also high-gradient boundary layer zone (Fig. 18). Computational domain is also considered large enough about one span in the upstream, downstream and lateral directions to minimize boundary effects and also to optimize the computational cost as shown in Fig. 18. After preliminary tests, finally an optimized mesh with about 2

million elements was selected to perform simulations.

To find physics of the problem, LB LRN $k-\varepsilon$ flow simulations were performed on the flipper geometry. Similar to the tubercled rectangular wing, flow field and forces in x and y directions are saved for post-processing with a total number of 18 simulations. For all numerical simulations, three components of the velocity are imposed as inflow boundary condition as before (3). All other settings are similar to the previous case (Section *A*.2).

2. Results

Fig. 19 shows performance curves of the flipper in the pre- and post-stall zones. As one can see in the figure, the humpback whale flipper desirably behaves in the post-stall region with maintaining lift coefficient about 1.3 up to $\alpha = 34°$ and higher than unity up to $\alpha = 40°$; superior maneuverability performance of humpback whales is majorly linked with this characteristics. Drag coefficient also monotonically increases over the AoA range and no oscillation is observed in the numerical prediction curve.
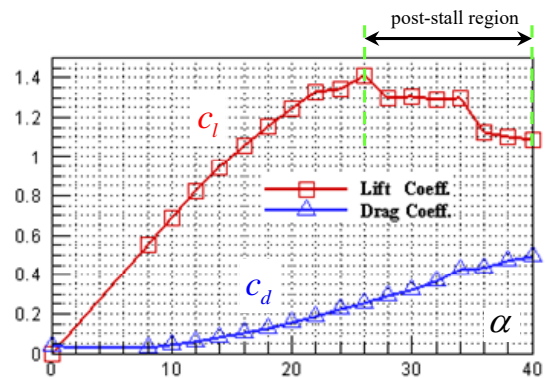

Fig. 19 Real humpback whale flipper performance curve

Flow pathlines over the flipper at $\alpha = 36°$ colored by axial velocity is also presented in Fig. 20. As one can see in the figure, two relatively large separation zones, starting from the middle plane of the wing to the wing tip, are generated on the top surface of the wing at this AoA. As shown in Fig. 19, a local drop in the lift coefficient happens at $\alpha = 36°$, linked with formation of this relatively large separation zone on the flipper model.

To gain a better insight about topology of the separation formation over the flipper by increasing AoA, top view of pathlines at different AoA is plotted in Fig. 21. As one can observe in the figure, at $\alpha = 18°$ flow is completely attached on the flipper surface and smooth pathlines exist downstream. By increasing AoA to $\alpha = 26°$, separation zones near the flipper tip starts growing and stream lines are also affected by presence of the separation zones. In this case, three separate vortical structures form at the downstream. By further increase in AoA to $\alpha = 32°$, separation region volume is getting bigger and extends up to the middle section of the flipper span. At $\alpha = 40°$, two distinct large separation regions are present on

the top surface of the flipper and four vortical structures are separately generated behind the flipper. These structures originate from the wing tip, wing root and separation regions. Ultimately, as one can see in the figure, at $\alpha = 50°$ separation zones merge on the wing planform and create an extensive separation region covering major portion of the wing surface. At this very high AoA, two distinct vortical regions linked with separated zones are getting merged and form a single vortical structure. In addition, tracer particle study has been performed in the case of humpback whale flipper. As before, ethane spherical particles with 0.0001 m diameter were utilized for this purpose. In this regard, tracer particles were continually released from the flipper surface. Similar to the tubercled rectangular wing, ideal reflection condition was applied for fluid particle-solid interactions.
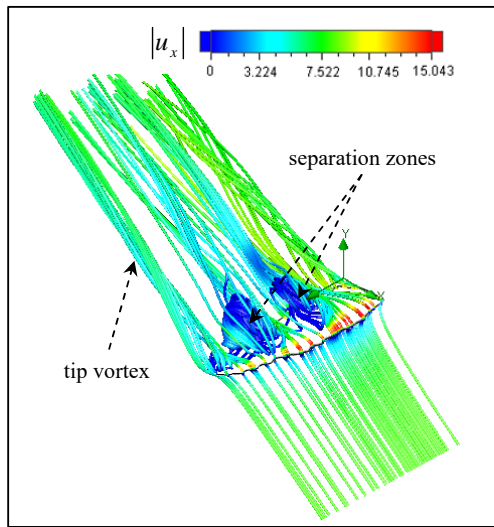

Fig. 20 Isometric view of flow pathlines over the humpback whale flipper model at $\alpha = 36°$

(a) $\alpha = 18°$

(b) $\alpha = 26°$

(c) $\alpha = 32°$
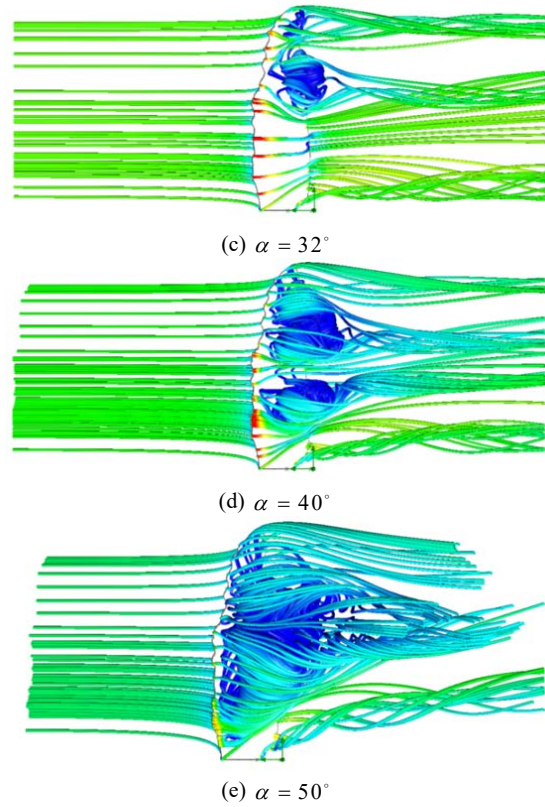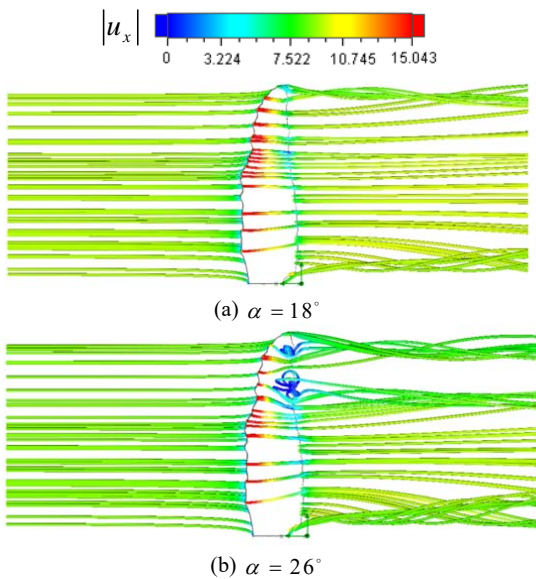

(d) $\alpha = 40°$

(e) $\alpha = 50°$

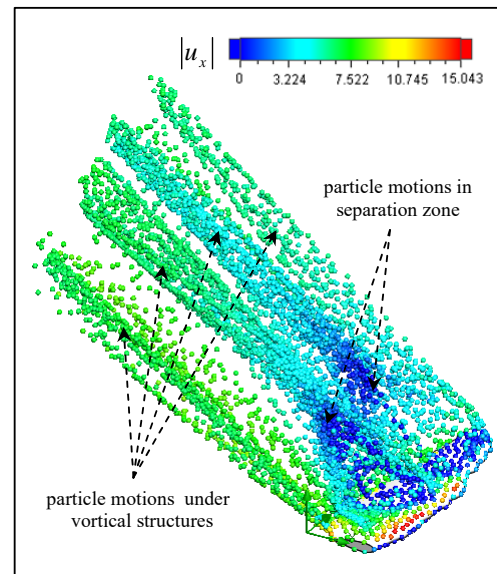Fig. 21 Top view of flow pathlines over the humpback whale flipper model at different AoAs

Fig. 22 Tracer particle dynamics over the humpback whale flipper model at high AoA, $\alpha = 40°$

Tracer dynamics on the flipper wing exhibit complicated motions induced by existing separation zones and vortical structures on the flipper wing. Fig. 22 shows a snapshot of the tracer motions colored by axial velocity of the particles at

$\alpha = 40°$. As shown in the figure and time-dependent motions of the particles, tracer particles outside of the separated region move in helical-like patterns under the four distinct vortical structures. On the other hand, particles inside the separation zone exhibit more complicated and semi-chaotic dynamical motions, which include first recirculating inside the separated region and then releasing and moving downstream under the existing vortical structures.

V. CONCLUSION

In this paper, a cascade-forward meta-model was designed based on the available experimental data on the rectangular tubercled planform in the literature to the date. As proven in the paper, the resulting trained ANN can be utilized as a fast and reliable tool inspired by humpback whale flipper geometry in the planform preliminary design phase. In addition, it was shown that the trained ANN can be coupled with any constrained optimization technique; in this regard, a zonal optimization strategy is recommended to obtain more accurate results. The methodology is also capable to include future experimental data by simply adding to its comprehensive database. In this way, accuracy of predictions on parameters in a given zone in the overall parameter-hyperspace improves by adding specific data. As an example, the strategy was applied in a case of a three parameter GA optimization with constrains. The amplitude and wavelength of the leading edge undulations were obtained for an optimized rectangular wavy planform in a given zonal space. Interestingly an optimum AoA was captured by the proposed ANN-GA strategy; at this AoA, a lift coefficient drop-off and drag coefficient oscillations are observed in the corresponding CFD simulation (in this case, $\alpha \approx 28°$) (Fig. 13).

Hydrodynamics of the sample optimized tubercled rectangular wing with finite span ($AR \approx 1$) along with a real humpback whale flipper model were assessed using LB LRN $k - \varepsilon$ flow simulations in SFS. In this regard, 3D geometry of the flipper model was constructed using SFS CAD, based on a real humpback whale planform [4]. Rib airfoil sections were considered as NACA 0021 and guideline curves were also fed into SFS as a cloud of points with high resolution. Computational grids around both tubercled wings were constructed using a Cartesian-based mesh in SFS along with an adaptive meshing near the solid immersed body to capture detail geometrical features of the tubercles as well as developing high-gradient boundary layers on the wing surface.

For the both tubercled wings, lift coefficient curves, obtained from the numerical simulations, showed a mild semi-flat and soft behavior in the post-stall region which maintains level of the lift coefficient after the stall point. This fact explains superior performance of the humpback whales in turning, rolling and banking maneuvers. The results also showed that in the case of the tubercled rectangular wing, due to low aspect ratio of the finite span wing and formation of separation zone at high AoA, tip-vortices are merged. Particle study in this case also revealed complicated dynamics of the flow particle motions induced by separation and vortical structures. In addition, streamline patterns in the trough and peak vertical planes exhibited a fully 3D flow on the tubercled wings.

The results also depicted that separation zones gradually form on the humpback whale flipper starting close to the wing tip by increasing AoA. A relative drop-off in lift coefficient in the post-stall region (Fig. 19) is also linked to the formation of these zones on the upper surface of the wing; although as mentioned before as superiority of the flipper performance, the tubercled flipper with its special topology creates a 3D flow structure that maintains lift at high AoA post-stall-region. In addition, as shown here, formation of the separation regions on the tubercled wing results in the formation of vortical structures behind the wing. For example, at $\alpha = 40°$, four distinct vortical structures are formed downstream behind the wing captured in the particle study, which originate from the wing tip, wing root and separation regions (Fig. 22). At high AoA, i.e. $\alpha = 50°$, vortical structures coming from separation zones are merged due to the separation zone merger already happened (Fig. 21 (e)). Finally, tracer particle dynamics study of the humpback whale flipper model at $\alpha = 40°$ revealed a chaotic pattern of particle motions induced by the separation zone and the four vortical structures (Fig. 22).

REFERENCES

[1] B.L. Woodward, J. P. Winn and F. E. Fish, "Morphological specializations of baleen whales associated with hydrodynamic performance and ecological niche", *Journal of Morphology*, vol.267, pp.1284–1294, 2006.
[2] Humpback whale documentation, *Marine Mammal Center*, Fort Cronkhite, Sausalito, CA.
[3] W. Welles, Picture Amy Whale, breaching, Stellwagen Bank National Marine Sanctuary, 2007.
[4] F.E. Fish and J. M. Battle, "Hydrodynamic design of the humpback whale flipper", *Journal of Morphology*, vol.225, No.1, pp.51–60, 1995.
[5] J. Potvin, J.A. Goldborgen, R.E. shadwick, "Passive versus active engulfment: verdict from trajectory simulations of lunge-feeding fin whales *Balaenoptera Physalus*", *Journal of the Royal Society Interface*, doi:10.1098/rsif.2008.0492, 2009.
[6] J. A. Goldbogen, J. Potvin and R.E. shadwick, "Skull and buccal cavity allometry increase mass-specific engulfment capacity in fin whales", *J. of Proceedings of the Royal Society B*, vol.277, pp.861–868, 2010.
[7] N. Rostamzadeh, K.L. Hansen, R.M. Kelso and B.B. Dally , "The formation mechanism and impact of streamwise vortices on NACA 0021 airfoils performance with undulating leading edge modification", *Journal of Physics of Fluids*, v.26, n.107101, 2014.
[8] K.L. Hansen, R.M. Kelso, B.B. Dally and E.R. Hassan, "Analysis of the streamwise vortices generated between leading edge tubercles", 6th *Australian Conference on Laser Diagnostics in Fluid Mechanics and Combustion*, Canberra, Australia, 5–7 December, 2011.
[9] K.Yang, L. Zhang and J.Z. Xu, "Simulation of aerodynamic performance affected by vortex generators on blunt trailing-edge airfoils", *Journal of Science China Technological Sciences, Springer-Verlag*, vol.53, no.1, pp.1-7, 2010.
[10] E.A. Van Nierop, S. Alben and M.P. Brenner, "How bumps on whale flippers delay stall: an aerodynamic model", *Physical Review Letters*, PRL 100, 054502, February 2009.
[11] A. Taheri, "On the hydrodynamic effects of humpback whale's ventral pleats", *American Journal of Fluid Dynamics*, vol.8, no.2, pp.47-62, 2018.
[12] J. Favier, A. Pinelli and U. Piomelli, "Control of the separated flow around an airfoil using a wavy leading edge inspired by humpback whale flippers", *Journal of Comptes Rendus Mecanique*, vol. 340, pp.107–114, 2012.
[13] H. Arai, Y. Doi, T. Nakashima and H. Mutsuda, "A Study on Stall Delay by Various Wavy Leading Edges", *Journal of Aero Aqua Bio-*

Mechanics, vol.1, no.1, pp. 18-23, 2010.

[14] C. Cai, Z. Zuo, S. Liu and Y. Wu, "Effect of a single leading-edge protuberance on NACA 63₄-021 airfoil performance", *ISROMAC 2016-International Symposium on Transport Phenomena and Dynamics of Rotating Machinery*, Hawaii- Honolulu, April 10-15, 2016.

[15] A.K. Malipeddi, "Numerical analysis of effects of leading edge protuberances on aircraft wing performance", *Master of Science Thesis, Department of Aerospace Engineering, Wichita State University*, 2011.

[16] A. Skillen, A. Revell, A. Pinelli, U. Piomelli and J. Favier, "Flow over a wing with leading-edge undulations", *AIAA Journal, American Institute of Aeronautics and Astronautics*, , vol.53, No.2 , pp.464-472, 2014.

[17] A. Esmaeili and J. M. M. Sousa, "Influence of wing aspect ratio on passive stall control at low Reynolds number using sinusoidal leading edges", *29ᵗʰ Conference of the International Council of the Aeronautical Sciences*, St. Petersburg, Russia, Sep. 7-12, 2014.

[18] K.R. Atkins, " Investigation into the flow behavior of a NACA 0021 airfoil with leading edge undulations simulated with RANS in STAR-CCM+", *School of Mechanical, Aerospace and Civil Engineering, Faculty of Engineering and Physical Sciences, University of Manchester*, UK.

[19] M. Asli, B. Mashhadi Gholamali and A. Mesgarpour Tousi, "Numerical Analysis of Wind Turbine Airfoil Aerodynamic Performance with Leading Edge Bump", *Journal of Mathematical Problems in Engineering*, Article ID 493253, 8 pages; http://dx.doi.org/10.1155/2015/493253, 2015.

[20] N. Rostamzadeh, R.M. Kelso, B.B. Dally and Z.F. Tian ,"An experimental and computational study of flow over a NACA 0021 airfoil with wavy leading edge modification", *18ᵗʰ Australasian Fluid Mechanics Conference*, Launceston, Australia, 3-7 Dec., 2012.

[21] C. Cai, Z. Zuo, S. Liu and Y. Wu, "Numerical investigations of hydrodynamic performance of hydrofoils with leading-edge protuberances", *Journal of Advances in Mechanical Engineering*, vol. 7, no.7, pp.1–11, 2015.

[22] I. Solís-Gallego, D. Menéndez-Alonso, A. Meana Fernández, J. M. Fernández Oro, K. M. Argüelles Díaz and S. Velarde-Suárez, "Optimization of Wind Turbine Airfoils using Geometries based on Humpback Whale Flippers", *International Congress of Energy and Environment Engineering and Management*, Paris, 22-24 July, 2015.

[23] T.M.A. Maksoud and V. Ramasamy, "The effect of leading edge and trailing edge protubercles on aerofoil performance", *HEFAT2014 10th International Conference on Heat Transfer, Fluid Mechanics and Thermodynamics*, Orlando, Florida, 14 – 16 July, 2014.

[24] J.H. Chen, S.S. Li and V.T. Nguyen, "The effect of leading edge protuberances on the performance of small aspect ratio foils", *15ᵗʰ International Symposium on Flow Visualization*, 25-28 June, Minsk, Belarus, 2012.

[25] H. T. C. Pedro and M. H. Kobayashi, "Numerical study of stall delay on humpback whale flippers", *46ᵗʰ AIAA Aerospace Sciences Meeting and Exhibit*, 7-10 January, Reno, Nevada, 2008.

[26] P. W. Weber, L. E. Howle, M. M. Murray and D. S. Miklosovic, "Computational Evaluation of the Performance of Lifting Surfaces with Leading-Edge Protuberances", *Journal of Aircraft*, vol. 48, no. 2, pp.591-600, 2011.

[27] M. W. Lohry, D. Clifton and L. Martinelli, "Characterization and design of tubercle leading-edge wings", *7ᵗʰ International Conference on Computational Fluid Dynamics (ICCFD7)*, Big Island, Hawaii, July 9-13, 2012.

[28] J. Joy, T.H. New and I. H. Ibrahim, "A computational study on flow separation control of humpback whale inspired sinusoidal hydrofoils", *International Journal of Mechanical, Aerospace, Industrial, Mechatronic and Manufacturing Engineering*, vol.10, no.2, 2016.

[29] D. Serson, J.R. Meneghini, S.J. Sherwin, "Direct numerical simulations of the flow around wings with spanwise waviness at a very low Reynolds number", *Journal of Computers and Fluids*, vol.146, pp.117–124, 2017.

[30] D.S. Miklosovic, M. M. Murray, L. E. H. and Fish, F. E., "Leading-edge tubercles delay stall on humpback whale (Megaptera novaeangliae) flippers", *Physics of Fluids*, vol. 16, pp. 39 – 42, 2004.

[31] D.S. Miklosovic, M. M. Murray and L. E. Howle, "Experimental Evaluation of Sinusoidal Leading Edges," *Journal of Aircraft*, vol. 44, no. 4, pp. 1404–1408, 2007.

[32] D. Custodio, "The effect of humpback whale-like leading edge protuberances on hydrofoil performance", *Master of Science Thesis, Department of Mechanical Engineering, Worcester Polytechnic Institute*, 2007.

[33] H. Johari, C. Henoch, D. Custodio and A. Levshin, "Effects of leading edge protuberances on airfoil performance", *AIAA Journal*, vol.45, no.11, pp.2634-2641, 2007.

[34] M. J. Stanway, "Hydrodynamic effects of leading edge tubercles on control surfaces and in flapping foil propulsion", *Master of Science Thesis, Department of Mechanical Engineering, Massachusetts Institute of Technology*, 2008.

[35] K. L. Hansen, "Effect of leading edge tubercles on airfoil performance", *Ph.D. Thesis, Department of Mechanical Engineering, University of Adelaide*, 2012.

[36] J. Borg, "The effect of leading edge serrations on dynamic stall*", M.S. Thesis, school of engineering sciences, Faculty of engineering and the environment, University of Southampton*, 2012.

[37] D. Custodio, C. Henoch and H. Johari, "Aerodynamic characteristics of finite span wings with leading edge protuberances", *AIAA Journal*, vol.53, no.7, pp. 1878-1893, 2015.

[38] A. Agrico de Paula, "the airfoil thickness effects on wavy leading edge phenomena at low Reynolds number regime", *Ph.D. thesis, Polytechnic school, University of Sao Paulo*, 2016.

[39] M.D. Bolzon, R.M. Kelso and M. Arjomandi, "The effects of tubercles on swept wing performance at low angles of attack", *19ᵗʰ Australasian Fluid Mechanics Conference Melbourne, Australia*, 8-11 December, 2014.

[40] M. Bolzon, R.M. Kelso, and M. Arjomandi. "Force measurements and wake surveys of a swept tubercled wing", *Journal of Aerospace Engineering*, Vol.30, No.3, 04016085, 2017.

[41] H.Demuth, M. Beale and M.Hagan, "Neural network toolbox user's guide", The MathWorks Inc., Natrick, USA, 2009.

[42] S. E. Fahlman and C. Lebiere, "The cascade-correlation learning architecture", *Advances in Neural Information Processing Systems*, no.2, pp. 524–532, 1990.

[43] A. Chipperfield, P. Fleming, H. Pohlheim and C. Fonseca, "Genetic Algorithm toolbox", Department of Automatic Control and Systems Engineering, University of Sheffield, 2000.

[44] SolidWorks, Software Package, Dassault Systemes, SolidWorks Corp., Concord, MA, 2016.

[45] A. Sobachkin and G. Dumnov, "Numerical Basis of CAD-Embedded CFD", *NAFEMS World Congress*, Dassult Systems Inc., 2013.

[46] C. K. G. Lam and K. A. Bremhorst, "A modified form of the k-e model for predicting wall turbulence", *Journal of Fluid Engineering*, Vol.103, pp. 456–460, 1981.